JOURNAL OF SPACECRAFT AND ROCKETS
Vol. 35, No. 4, July–August 1998

Viscous/Inviscid Interactions of the Forebody Flowfield of an Airbreathing Hypersonic Vehicle

John J. Bertin,* Matthew C. Towne,† Mark A. Malan,‡ Alois F. Kreins,§ Matthew E. Zuber,¶ and Michael B. Parks‡
U.S. Air Force Academy, USAF Academy, Colorado 80840

A hypersonic cruise missile, which can be launched from conventional aircraft or from surface-based assets and which can cruise at a Mach number of 8, requires at least two propulsion systems: a rocket-based propulsion system and a supersonic combustion ramjet system. The inlet to the airbreathing propulsion system will be closed during that portion of the flight powered by the rocket-based propulsion system. As a result, a shock-wave/boundary-layer interaction will result when the supersonic flow on the forebody encounters the compression ramp formed by the closed inlet. To investigate the flowfield for this interaction, surface-pressure measurements and flow-visualization photographs have been obtained during an experimental program conducted in the Tri-Sonic Wind Tunnel at the U.S. Air Force Academy. Data were obtained at a freestream Mach number of 4.28 and at a freestream Reynolds number (based on the model length) of 12.79 $\times$ 10^6 over an angle-of-attack range from −7.3 to +7.3 deg. The data are compared with computations made with version 3 of the General Aerodynamic Simulation Program. The three-dimensional viscous/inviscid interaction that occurs near the compression ramp contains transverse vortices and streamwise vortices, with pressures in the reattachment region being approximately an order of magnitude larger than those for the undisturbed flow upstream of the interaction.

Nomenclature

h = height of the airbreathing engine flowpath, 0.28 in.; see Fig. 2
M = Mach number
p = static pressure, psia
p_{or6} = static pressure measured at orifice 6, psia
p_{t1} = total pressure in the tunnel reservoir, psia
s = wetted distance measured from the leading edge of the compression surface, i.e., the nose of the model, in.; see Fig. 2
s_0 = wetted length from the leading edge of the compression surface to the upstream edge of the compression ramp, 5.50 in.; see Fig. 2
s' = wetted distance measured in the upstream direction starting from the upstream edge of the compression ramp, in.; see Fig. 2
T_{t1} = total temperature in the tunnel reservoir, °R
V = velocity, ft/s
x, y, z = coordinate system for the GASPv3 computations, in.
x_0 = X-coordinate distance from the leading edge of the compression surface to the upstream edge of the compression ramp, 5.46 in.; see Fig. 2
y = distance from the plane of symmetry, in.; see Fig. 2
y_f = y distance from the plane of symmetry to the vertical side of the engine flow path, 0.84 in.; see Fig. 2
α = angle of attack, deg
γ = ratio of specific heats
μ = viscosity, lbf s/ft^2
ρ = density, slugs/ft^3
ω = absolute humidity

Subscript

1 = freestream conditions

Introduction

ADDRESSING the questions of which Air Force missions are best accomplished by hypersonic vehicles and which technologies are required to design and to build these vehicles, a senior aeronautical engineering design class at the U.S. Air Force Academy (USAFA) developed a concept for a hypersonic attack platform.[1] One component of this integrated weapons system is a stand-off hypersonic missile with attack capability (SHMAC). This hypersonic cruise missile (HCM) could be launched from a surface-based asset (such as a launch system on a naval ship or an army launcher), from a conventional aircraft (such as an F-15), or from a hypersonic strike aircraft (which is another component of the integrated weapons system). Cruising at a nominal Mach number of 8, the HCM is capable of striking targets 1000 n miles away in 15 min, without placing the launch platform or its crew in harm's way. For cruise, the SHMAC is powered by a supersonic combustion ramjet (scramjet), which is an airbreathing propulsion system. By limiting the maximum Mach number for cruise to approximately 8, one can use endothermic hydrocarbon fuels, as opposed to liquid hydrogen, because the high-heat-sink capacity of hydrogen is not required. The endothermic hydrocarbon fuels are attractive because they greatly simplify ground maintenance and logistics support requirements. However, if the missile is to be launched from a surface-based asset or from a conventional aircraft, another propulsion system is needed to accelerate the missile from the launch conditions to the speeds required for the efficient operation of a scramjet. The other propulsion system is a rocket that is located in the airbreathing propulsion system's flowpath and is ejected (casing and all) once the conditions required for efficient operation of the scramjet are achieved. Because it is this phase of the SHMAC mission that is of primary interest to the present investigation, i.e., when the HCM is powered by the rocket, the inlet to the scramjet flowpath will be closed.

Following the guidelines developed during the Aerodynamic Configured Missile program,[2] to have an adequate lift-to-drag ratio, the shape of the configuration should have a noncircular cross section, a large planform area, and a flat bottom. The SHMAC configuration is presented in Fig. 1. A slightly divergent platypus (or shovel-like) nose formed a compression surface upstream of the inlet of the airbreathing propulsion system. Recall that the phase of flight of primary interest to this investigation is that powered by the

---

Presented as Paper 97-0766 at the AIAA 35th Aerospace Sciences Meeting, Reno, NV, Jan. 6–10, 1997; received Jan. 20, 1997; revision received Jan. 15, 1998; accepted for publication April 8, 1998. This paper is declared a work of the U.S. Government and is not subject to copyright protection in the United States.

*Professor of Aeronautics, Department of Aeronautics. Fellow AIAA.

†Assistant Deputy for Operations, Department of Aeronautics. Senior Member AIAA.

‡Cadet First Class, Department of Aeronautics.

§Visiting Scholar, Department of Aeronautics. Member AIAA.

¶Research Engineer, Department of Aeronautics. Student Member AIAA.

rocket-propulsion system. Thus, the inlet to the flowpath of the air-breathing propulsion system is closed, forming a compression ramp to the oncoming flow. When the shock-wave system associated with the ramp-induced turning of the flow interacts with the approach boundary layer, a strong viscous/inviscid interaction occurs. Because these interactions produce locally severe surface pressures and heat transfer rates, understanding them is critical to the design of hypersonic vehicles. Thus, they have been the subject of numerous investigations, e.g., Refs. 3–6, and of symposia, e.g., Ref. 7.

An experimental program has been conducted in which surface-pressure measurements, oil-flow patterns, and schlieren photographs were obtained for a model exposed to a Mach 4.28 airstream. These data are compared with computations made using version 3.0 of the General Aerodynamic Simulation Program (GASPv3).[8] In addition, the data are analyzed to develop an empirically based understanding of the viscous/inviscid interaction flowfield.

Experimental Program

The experimental investigation utilized the USAFA's Tri-Sonic Wind Tunnel (TWT), which is a blowdown facility that discharges to the atmosphere. Reference 9 contains more information about the facility.

Test Conditions

The freestream Mach number in the test section was 4.28 ± 0.04. This Mach number is the average value determined from a facility calibration program in which an 11-probe pitot rake was rotated in 30-deg increments. These pitot-pressure measurements were used to generate Mach number contours for three planes in the test section: one at the upstream end, the second in the middle, and the third at the downstream end of the test section. This value has been verified in repeated investigations of the flow quality of the TWT.

All of the data were obtained at one nominal test condition: $p_{t1} = 150$ psia and $T_{t1} = 547.5°\text{R}$. The greatest variation in the stagnation conditions for a single run occurred during the longest duration run of the test program. During this run, p_{t1} varied from 149.93 to 150.29 psia and T_{t1} varied from 545.7 to 552.0°R. Over the entire test program, p_{t1} varied from 149.67 to 150.38 psia and T_{t1} varied from 542.4 to 552.7°R.

The perfect-gas relations were used to calculate the freestream conditions, assuming that the flow accelerated isentropically from the nominal stagnation conditions to the Mach 4.28 freestream. Sutherland's equation[10] was used to calculate the freestream viscosity. As a result, the freestream unit Reynolds number is 12.18×10^6/ft. The freestream Reynolds number based on the length of the model is 12.79×10^6. However, as noted in Ref. 10, "One would expect that the actual viscosity is 3 percent to 5 percent greater than Sutherland's value" at the temperatures characteristic of the freestream flow in a supersonic/hypersonic wind tunnel.

During the investigations of the flow quality in the TWT, it was found that the freestream flow was not perfectly aligned with the tunnel axis. The flow misalignment is approximately +0.5 deg in the pitch plane and +0.5 deg in the yaw plane.

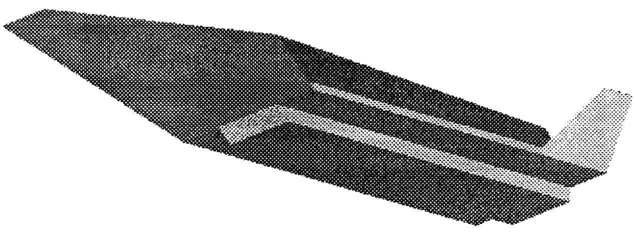

Fig. 1 SHMAC.

Model

A three-view, dimensioned diagram of the SHMAC wind-tunnel configuration is presented in Fig. 2. The overall length of the wind-tunnel configuration is 12.60 in. Because a typical hypersonic cruise missile designed for launch from an F-15 is approximately 160 in. long, the scale of the wind-tunnel model is approximately 0.079. There were actually two wind-tunnel models built (to the same dimensions) for these wind-tunnel tests. The first model (SHMAC-I) was built with relatively limited instrumentation so that it would be ready for use in the senior aeronautical engineering design class to complement the mission study.[1] The locations of 17 pressure orifices on the SHMAC-I model are shown in Fig. 2. Note that none of the 12 orifices in the vicinity of the compression ramp of the SHMAC-I was located in the plane of symmetry. Because the oil used to obtain oil-flow patterns over the SHMAC-I fouled the pressure lines, a second model was built (SHMAC-II). This model had additional orifices (a total of 30) to better define the flow in the plane of symmetry and in the interaction region.

The coordinate systems are shown in Fig. 2. The coordinates of the five orifices that are on the forebody compression surface well upstream of the viscous/inviscid interaction region (associated with the compression ramp) are given in terms of the dimensionless distance from the nose of the model (s/s_0) and the dimensionless distance from the plane of symmetry (y/y_f). The coordinates of the 12 orifices located just upstream of the compression ramp formed by the closed inlet are given in terms of the dimensionless distance from the leading edge of the compression ramp (s'/h) and of the dimensionless distance from the plane of symmetry (y/y_f).

Instrumentation

The static pressures acting on the model surface were transmitted through a pressure orifice formed by stainless-steel tubing, which had an inside diameter of 0.0310 in. and was mounted flush to the model surface. The pressures then passed through approximately 10 ft of Tygon® tubing, which had an inside diameter of 0.0313 in. and an outside diameter of 0.0938 in., to a Scanivalve®, which housed the pressure transducer. For the present tests, a Kulite® differential-pressure transducer with a full-scale range of 15 psi differential and a combined nonlinearity and hysterises of ±0.5%

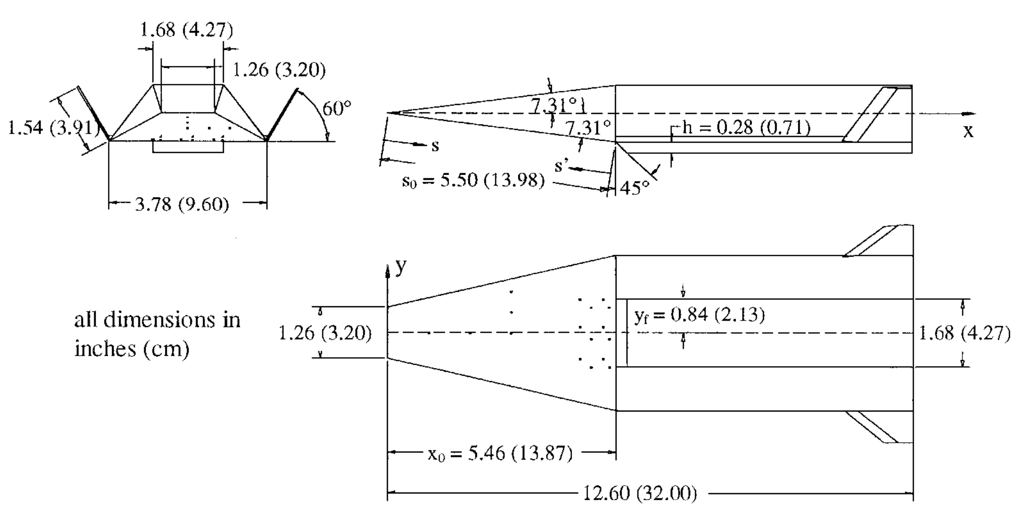

Fig. 2 Three-view diagram of the SHMAC wind-tunnel model.

full scale was used to measure the gauge pressure relative to the static pressure in the Aeronautical Research Center. The reference (atmospheric) pressure was measured by a Heise digital pressure indicator with a full-scale range of 17.19 psia. Including the effects of sensitivity, hysterises, nonlinearity, and repeatability, the atmospheric pressure measurement had an uncertainty of ±0.035% of the full-scale measurement at 70°F.

Because of the long length of Tygon tubing connecting the pressure orifice in the model to the Scanivalve/transducer, all pressure measurements were time-averaged, steady-state values. Once the flow was established, there was a 3000-ms delay before the first pin of the Scanivalve was recorded. There was a 200-ms delay between each of the subsequent steps. Dolling[11] noted that the instantaneous pressure in the interaction region of a two-dimensional ramp flow is in reality intermittent, jumping randomly back and forth from the range characteristic of the undisturbed boundary layer to a higher level corresponding to flow downstream of the separation shock. The average pressure is generated by the superposition of very large-amplitude fluctuations on the undisturbed boundary-layer pressure signal and increases in the downstream direction because the intermittency progressively increases.

Uncertainty and Repeatability

The experimental pressures are usually presented as the pressure measurement for a particular orifice p divided by the calculated value of the freestream static pressure p_1, yielding the dimensionless pressure parameter p/p_1. A typical value of the pressure measured at the orifice located at an s of $0.545 s_0$ in the plane of symmetry is 1.400 psia. Let us assume that the freestream Mach number is 4.28 and that the stilling chamber pressure p_{t1} is 150.0 psia. The corresponding value of p_1 is 0.6848 psia, and the value for the dimensionless parameter for the pressure measurement is 2.044.

The measured pressure is determined as the sum of the differential pressure sensed by the Kulite pressure transducer located in the Scanivalve and the atmospheric pressure given by the Heise digital pressure indicator:

$$p = \Delta p_{\text{Kulite}} + p_{\text{atm}} \tag{1}$$

For the present example, the differential pressure sensed by the Kulite transducer is -9.800 ± 0.075 psig and the atmospheric pressure is 11.200 ± 0.006 psia. Combining the extremes of the uncertainties, the measured pressure could be as high as 1.481 psia or as low as 1.319 psia. Thus, the measured pressure at this orifice (which is in a region of the model unaffected by viscous/inviscid interactions) is 1.400 psia ±5.8%.

Because the freestream static pressure p_1 is calculated using

$$p_1 = (p_1/p_{t1})p_{t1} = \left(\left\{1 + [(\gamma - 1)/2]M_1^2\right\}^{-\gamma/(\gamma-1)}\right)p_{t1} \tag{2}$$

there are two sources of uncertainty: the uncertainty in the pressure ratio because the freestream Mach number can be as low as 4.24 or as high as 4.32 and the uncertainty in the stagnation pressure measurement itself. Combining the extremes of the uncertainties, the calculated value of p_1 could be as high as 0.7252 psia or as low as 0.6466 psia. Thus, the reference pressure is 0.6848 psia $+5.9\%/-5.6\%$. Using the approach of Kline and McClintock,[12] the uncertainty in calculating the reference pressure is ±5.8%.

Combining these results, for this hypothetical case, p/p_1 could be as low as 1.818 or as high as 2.290, which represents an uncertainty band of $+12.0\%/-11.1\%$ about the nominal value of 2.044. However, if one neglects the uncertainty in the freestream pressure due to the uncertainty in the freestream Mach number, the uncertainty in p/p_1 is approximately ±6%.

Surface pressure measurements with the model at essentially zero angle of attack were obtained during three different runs of the SHMAC-II phase of the test program. For two of the runs, a locking device was placed in the angle-of-attack mechanism so that the model-mounting sting could not move during the run. For the third run, the model was at 0.1-deg angle of attack, and the locking mechanism was not in place. Because the locking mechanism could be not be used for those runs where data were to be obtained at nonzero angles of attack, the third run was more like a typical run. The pressure measurements from these three runs are presented in Fig. 3 for all 30 orifices of the SHMAC-II model. Note that all of the calculations of p_1 assume that the freestream Mach number is 4.28. Thus, the uncertainty in the freestream Mach number is not included in the calculation of the value of the dimensionless pressure parameter p/p_1. The values of the pressure parameter for orifice 5 (which is at an s of $0.545 s_0$ and, therefore, corresponds to the hypothetical case described in the preceding paragraphs) range from 1.944 to 2.019. Thus, the variation between the lowest value and the highest value of p/p_1 for orifice 5 is less than 4%. This repeatability is typical of the measurements for those orifices located in regions not affected by viscous/inviscid interactions. Thus, the experimentally determined variations in the pressure parameter for a series of three repeat runs are significantly smaller than bounds given by the uncertainty analysis.

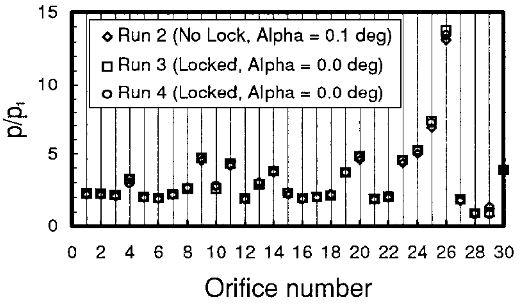

Fig. 3 Dimensionless pressure parameter for three runs at zero angle of attack, illustrating the repeatability of the data.

The largest variations in the values of the pressure parameter from the three runs occur in regions affected by the viscous/inviscid interactions. For the three orifices located on the face of the closed inlet, i.e., on the compression ramp, the variation between the lowest value and the highest value of p/p_1 for a particular orifice is less than 8%. This relatively large run-to-run variation in the experimental values of the pressure parameter on the compression ramp is not surprising, because slight changes in the location of the reattachment streamline can produce large variations in the pressure at a specific location. Thus, slight variations in the flow physics can produce variations in the pressures measured at a particular orifice that are much greater than the variations associated with the measurements themselves.

Numerical Analysis

Using GASPv3 (Ref. 8), the flowfield for the plane of symmetry of the engine side of the model was computed for the thin-layer Navier–Stokes (TLNS) equations. The TLNS equations are numerically solved using a finite volume formulation. GASP offers numerous solution options to the user. The inviscid flux vectors were computed to second-order accuracy using van Leer's flux vector splitting technique combined with the min–mod limiter to maintain stability and eliminate numerical oscillations in regions containing large gradients. The two-factor approximate factorization time-integration scheme was used to solve the TLNS equations. Solutions were considered converged when the residual had decreased by three orders of magnitude.

Numerical solutions for the plane-of-symmetry flow were generated using a two-dimensional model for the flow. Although this is not a rigorous flow model, the use of the two-dimensional approximation to compute the plane-of-symmetry viscous/inviscid interactions in the vicinity of a compression ramp is common.[3–5] Thomas et al.[6] studied surface pressure measurements in the vicinity of a two-dimensional ramp. Because the experimental data were obtained on a plate with a spanwise width of 2 ft but with no side plates to constrain the flow, Thomas et al.[6] considered the possibility that three-dimensional effects were significant for flow over this two-dimensional model. The pressure contours in the downstream plane on the ramp indicated an expansion of the flow in the spanwise direction near the edge of the plate. The three-dimensional effects produced a smaller separated-flow region in the centerplane than that predicted using the two-dimensional calculations. The time variation of the computed three-dimensional flowfield indicated that

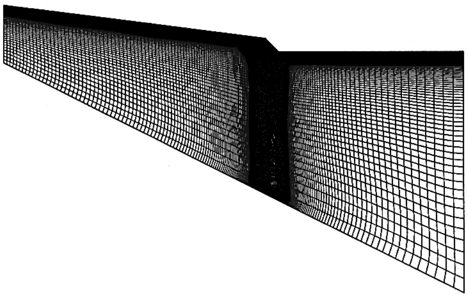

Fig. 4 Engine side of SHMAC 257 × 129 grid.

the steady-state flow is achieved in approximately 4 ms, which is in agreement with the experiment. Thus, the extent of and the time to establish the separation for this flow are strongly influenced by three-dimensional effects. For the present tests, the principal objectives of the comparisons between the computed parameters and the measured parameters include establishing the credibility of the measurements and gaining insights into the flow physics. Thus, that the flow is not actually two dimensional should be noted but is not considered critical.

When computing the flowfield, the freestream flow conditions were specified at the inflow and at the far-field boundaries. A second-order extrapolation boundary condition was specified for the downstream, outflow boundary. Boundary conditions at the surface of the vehicle included a no-slip requirement for the velocity boundary condition. The thermal boundary condition at the wall was either a specified temperature or there was no heat-transfer to the wall, i.e., the adiabatic-wall condition. Thus, the computations were made for boundary conditions, e.g., wall temperature, the freestream flow, etc., that matched the actual wind-tunnel test conditions as closely as possible.

For the computation of the plane-of-symmetry flow on the engine side of the model, the grid was created using a grid generation code.[13] As indicated in Fig. 4, there were 257 nodes along the body and 129 nodes from the body to the outer boundary. The far-field boundaries were placed far enough from the vehicle to capture the attached shock wave emanating from the leading edge of the SHMAC. The distance to the first grid point off the surface is nominally $0.000022x_0$.

Because measurements of the surface temperature were not made as part of the experimental program, flowfield computations were made for a range of realistic thermal boundary conditions. At the start of a run, the model is at room temperature, which is approximately 530°R. The model cooled during the run, approaching the recovery temperature for long-duration runs. Thus, flowfield solutions were computed for three different thermal boundary conditions: an adiabatic wall, and constant wall temperatures of 500 and of 530°R. The pressure distributions for the flowfield computed for these three different thermal boundary conditions are presented in Fig. 5a. These computations indicate that, over the range of surface temperatures of interest to the present study, the surface temperature has only a relatively small effect on the surface pressures in the shock-wave/boundary-layer interaction region. As one might expect, the surface pressures upstream of the interaction region are unaffected by the surface temperature.

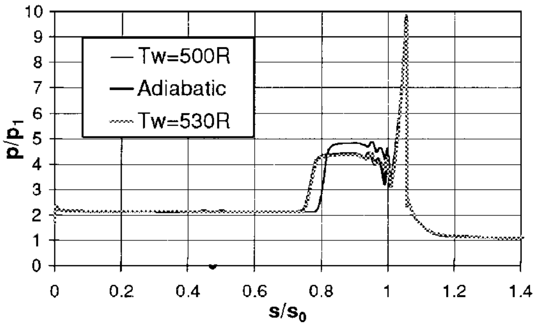

a) Effect of the thermal boundary conditions; Baldwin–Lomax turbulence model

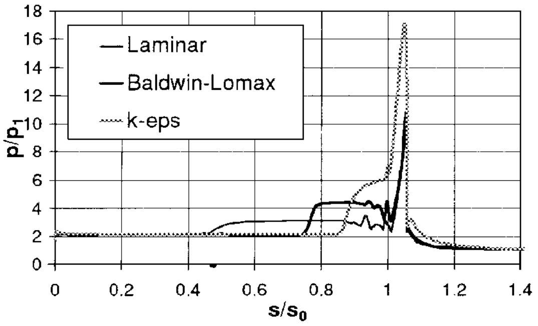

b) Effect of the boundary-layer model; T_w = 530°R

Fig. 5 Surface-pressure distributions from the plane of symmetry of the engine side using various options in the GASPv3 computed flowfields for zero angle of attack.

No measurements were made during the present program to locate the onset of boundary-layer transition. However, assuming that the flow at the edge of the boundary layer was that for a 7.31-deg wedge, the unit Reynolds number of the inviscid flow is 15.39×10^6/ft. Thus, the Reynolds number, based on the local flow properties and on s_0 (the wetted length from the leading edge of the compression surface to the upstream edge of the compression ramp) is 7.06×10^6. Based on these values of the Reynolds number, one would expect that boundary-layer transition would occur well upstream of the compression ramp. Nevertheless, flowfield computations were made assuming both that the boundary layer remains laminar and that the boundary layer is turbulent from the leading edge. Two turbulence models were used to represent a range of models available in codes such as GASPv3. The algebraic Baldwin–Lomax model[14] divides the boundary layer into an inner region and an outer region. The two equations of the k–ε turbulence model[15] are those for turbulent kinetic energy k and its dissipation ε. The corresponding pressure distributions for these three boundary-layer models are presented in Fig. 5b.

The computations indicate that, if the boundary layer were laminar, the shock-wave/boundary-layer interaction (and boundary-layer separation) would occur well upstream of the compression ramp. The measured pressures and oil-flow patterns indicate that this is definitely not the case. Furthermore, as discussed earlier, the Reynolds number would lead one to expect that transition would occur not far from the nose. Thus, it is not realistic to assume that the boundary layer is entirely laminar. In the subsequent Discussion of Results section, computed pressure distributions for the two-dimensional flowfields will be presented only for the two turbulence models and for a single surface temperature, 530°R.

Discussion of Results

Measurements from the Plane of Symmetry

Pressure distributions for the plane of symmetry on the engine side of the model at zero angle of attack are presented in Fig. 6 in terms of the dimensionless pressure parameter p/p_1. The measurements are from the three repeat runs that were originally discussed in Fig. 3. Included for comparison are the computations made using the Baldwin–Lomax turbulence model and the k–ε turbulence model. The pressure measurements near the nose of the model are in very close agreement with the values computed assuming that the flow is two dimensional. The pressures measured at an s of $0.545s_0$ and of $0.727s_0$ are slightly below the two-dimensional predictions. Because Mach waves propagating from the edges of the model would intersect the plane of symmetry near $s = 0.50s_0$, the pressures measured at these two orifices are believed to be affected by three-dimensional effects.

A significant streamwise increase in the experimental pressures occurs beginning at an s of approximately $0.85s_0$, indicating the leading edge of the λ shock wave associated with the shock-induced viscous/inviscid interaction. As can be seen in Fig. 6, this location is approximately the same as the location where the pressures predicted using the k–ε turbulence model first begin to increase. The accumulation of oil determined from oil-flow patterns, such as

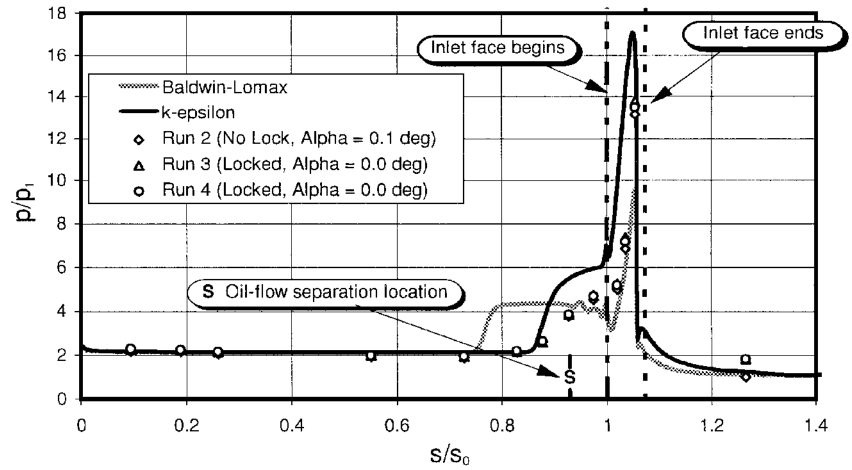

Fig. 6 Pressure distributions for the plane of symmetry on the engine side of the model at zero angle of attack.

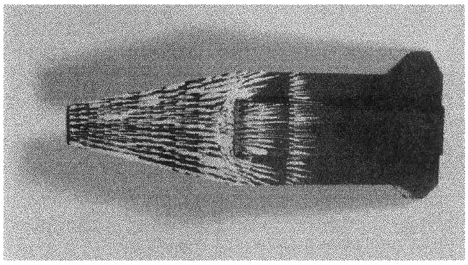

Complete model

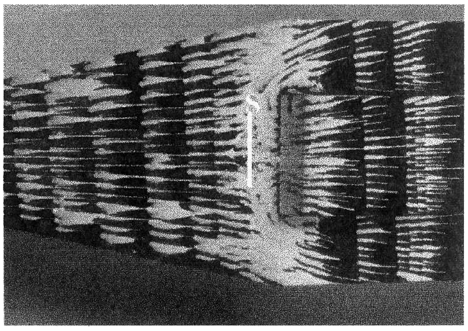

Close-up of oil-flow pattern for the interaction region

Fig. 7 Oil-flow pattern for the SHMAC-I at zero angle of attack.

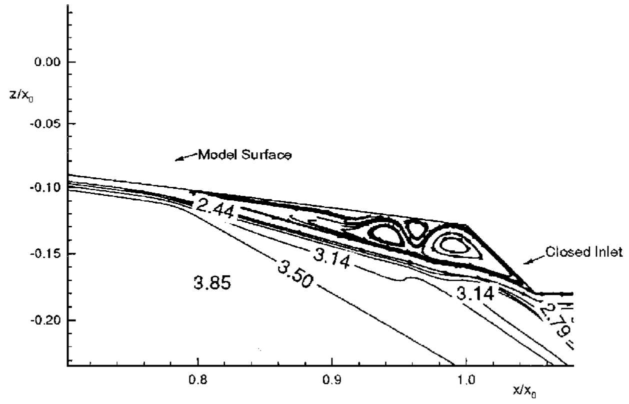

Baldwin–Lomax turbulence model

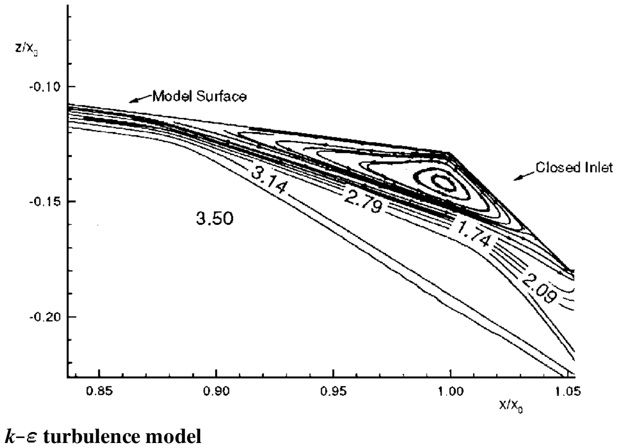

k–ε turbulence model

Fig. 8 Computed Mach number contours and streamlines for the separation region; $\alpha = 0$ deg, $T_w = 530°$R.

presented in Fig. 7, can be used to determine the upstream limit of the reverse flow on the surface of the model. Based on the oil-flow pattern, separation occurs in the plane of symmetry at an s of $0.92s_0$. Refer to the "S" located just above the abscissa in Fig. 6. Thus, the surface-pressure measurements, the flowfield computed using the k–ε turbulence model, and the oil-flow patterns all indicate similar locations for the leading edge of the shock-wave/boundary-layer interaction.

The streamwise increase in the pressure distribution and, therefore, the leading edge of the interaction region for the flowfield computed using the Baldwin–Lomax[14] turbulence model begin at an s of approximately $0.77s_0$ for zero angle of attack. Because of the increased length of the separation region when the Baldwin–Lomax turbulence model is used, the flow at the leading edge of the interaction turns through a smaller angle than for the k–ε solution. Streamlines in the separation region and Mach number contours for the interaction region, when the model is at zero angle of attack, are compared in Fig. 8 for the two turbulence models. For a smaller turning angle, the leading edge of the λ shock wave has a smaller inclination angle, the Mach number downstream of this shock wave is higher, and the static pressure in the separation region upstream of the compression ramp is lower. The effects of these phenomena are shown in the data and in the computations presented in Figs. 6 and 8. Note that the pressure measurements on the flat surface just upstream of the compression ramp more closely follow the k–ε computations (see Fig. 6). As indicated in Fig. 8, multiple transverse vortices form in the extended length of the separation bubble computed using the Baldwin–Lomax turbulence model, whereas there is only a single transverse vortex evident in the k–ε solution. A concerted effort was made when obtaining oil-flow patterns to determine whether there was evidence of multiple vortices on the model surface in the separation region upstream of the compression region. No clear indication of a multiple-vortex pattern was observed in any of the oil-flow patterns.

On the face of the compression ramp itself, the measured pressures more nearly match the Baldwin–Lomax computations. The maximum pressure measured on the compression ramp is between the peak value computed using the Baldwin–Lomax[14] turbulence model and that computed using the k–ε turbulence model.

There are several potential reasons for the differences between the experimental and the computed values for the surface pressures, including the unsteady nature of the flow, three-dimensional effects, and the turbulence model. The unsteady nature of the compression-ramp flowfield is well documented, e.g., Ref. 4. Dolling[11] noted that, "Although some steady-state computations may reproduce certain flowfield properties reasonably well, such comparisons can only be regarded as fortuitous since the underlying physics is not modeled. Without modeling the unsteadiness, predicting the correct surface and flowfield properties will remain elusive, irrespective of the turbulence model."

However, as noted earlier, all pressure measurements in the present program are time-averaged, steady-state values. They are compared with pressures from steady-state flowfield computations. Recall that Thomas et al.[6] considered the possibility that three-dimensional effects were significant to surface-pressure measurements that were obtained on a two-dimensional ramp. The pressure contours in the downstream plane on the ramp indicated an expansion of the flow in the spanwise direction near the edge of the plate. The three-dimensional effects produced a smaller separated-flow region in the centerplane than that predicted in the two-dimensional calculations. Thus, there are three-dimensional effects evident in the flowfield for a model that is intended to produce a two-dimensional flowfield.

Wilcox[16] cites a persistent lack of success in any one turbulence model producing computational fluid dynamics solutions for the compression-corner flowfield. The principal objectives of the comparisons between the computed parameters and the measured parameters in the present program include establishing the credibility of the measurements and gaining insights into the flow physics. However, the present data do not provide the kind of information that is required to modify the turbulence models should deficiencies be found. Furthermore, as noted by Wilcox,[16] "Algebraic models are the simplest and easiest to implement of all turbulence models. They are conceptually very simple and rarely cause unexpected numerical difficulties. Because algebraic models are so easy to use, they should be replaced only when demonstrably superior alternatives are available." Because no clearly superior model was found for this effort, the numerical pressure distributions used in the subsequent comparisons with measurements will be from the flowfield solutions using the Baldwin–Lomax[14] turbulence model.

Pressure distributions for the plane of symmetry on the engine side of the model are presented in Fig. 9 in terms of the dimensionless pressure parameter p/p_1 for angles of attack of −7.3 and +7.3 deg. Included for comparison are the computed pressure distributions using the Baldwin–Lomax[14] turbulence model. The comments made regarding the zero-angle-of-attack correlations presented in Fig. 6 apply to these data with one exception. The difference between the measured and the (two-dimensional) computed pressure distribution for an angle of attack of +7.3 deg indicates that the flow is three dimensional starting at the nose of the model and proceeding downstream to the interaction region.

Experimental values of the dimensionless pressure parameter for the orifice at an s of $0.545s_0$ are presented in Fig. 10 as a function of the angle of attack. Data are presented from both the SHMAC-I and the SHMAC-II programs. The measurements from the two programs (which were six months apart) are in good agreement. Included for comparison are the theoretical values for inviscid flow of perfect air past a two-dimensional wedge.[17] When alpha is −7.3 deg, the forebody surface on which the pressure orifice is located is parallel to the oncoming freestream, i.e., the deflection angle is zero. When the angle of attack is −7.3 deg, the measured pressure is in excellent agreement with the theoretical value, which assumes a two-dimensional flow. However, there is a difference between the measured pressures and the theoretical values, which increases as the angle of attack is increased. The growing difference is attributed to three-dimensional effects, which increase as the angle of attack increases. Recall from the discussion of the pressure distributions in Fig. 9 that, when the angle of attack is +7.3 deg, the flow is three dimensional starting at the nose and proceeding downstream to the interaction region.

Measurements from the Interaction Region

Presented in Fig. 11 are the pressure measurements from the orifices just upstream of the compression ramp that represents the closed inlet. The orifice numbers are identified in Fig. 11. The experimental values are presented as p/p_{or6}, which is the ratio of the pressure measured at the orifice of interest divided by the pressure measured at orifice 6, which is located in the plane of symmetry at an s of $0.727s_0$. Referring to the pressure distributions presented in Figs. 6 and 9, orifice 6 is the most downstream orifice that is not affected by the viscous/inviscid interaction for the entire angle-of-attack range. Thus, p/p_{or6} (which is the vertical length of the bars in Fig. 11) represents the ratio of the pressure at the orifice of interest to the undisturbed pressure upstream of the interaction. The maximum value of this perturbed pressure ratio was usually sensed at orifice 9

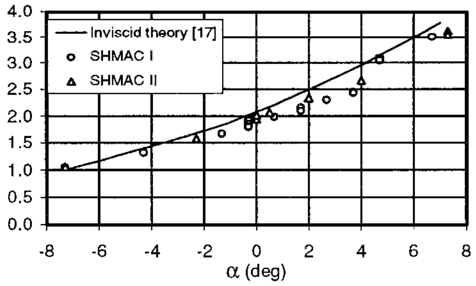

Fig. 10 Dimensionless pressure parameter at $s = 0.545s_0$ as a function of the angle of attack.

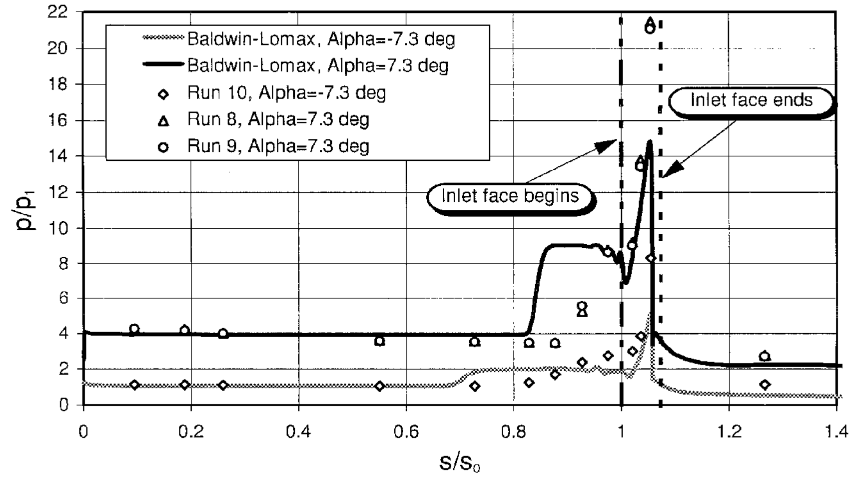

Fig. 9 Pressure distributions for the plane of symmetry on the engine side of the model at $\alpha = 7.3$ and −7.3 deg.

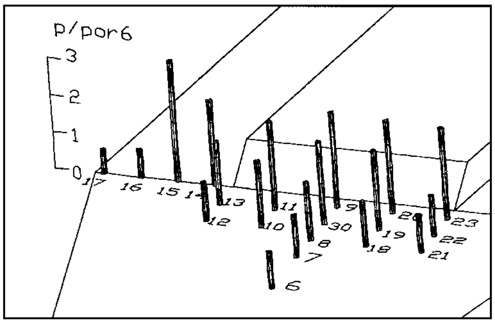

a) $\alpha = -7.3$ deg

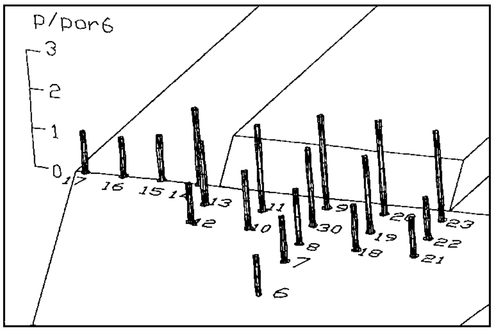

b) $\alpha = 0$ deg

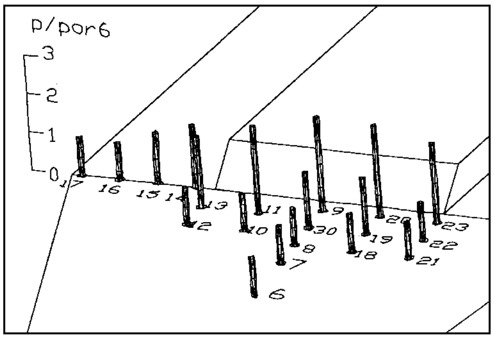

c) $\alpha = +7.3$ deg

Fig. 11 Perturbed pressure ratio for the orifices located in the interaction region.

(the orifice in the plane of symmetry, nearest the leading edge of the compression ramp) and was approximately 2.5 for all three angles of attack. The one exception to the maximum value occurring at orifice 9 was the relatively high value (3.253) that occurred for an alpha of −7.3 deg (see Fig. 11a) at orifice 15 (an orifice in the plane of the leading edge of the compression ramp). Apparently, the shock wave produced by the presence of the compression ramp passed over this orifice, producing this relatively high value for the perturbed pressure ratio. The pressures in the row nearest the leading edge of the compression ramp exhibit a slight decrease from the peak value at orifice 9. The pressures in the middle row exhibited a strong dependence on y, with the pressure at the orifice located at $y = y_f$ being approximately equal to the undisturbed pressure at all three angles of attack. The values of the perturbed pressure ratio for the orifices in the most upstream row, i.e., an s' of $2.5h$, were very sensitive to the angle of attack. For an alpha of +7.3 deg, the pressures in this row were essentially equal to the pressure in the undisturbed flow upstream of the interaction (see Fig. 9). For an alpha of −7.3 deg, the pressures in this row were well above the undisturbed value. Thus, these data indicate that the upstream extent of the interaction decreased as the angle of attack increased. This trend is consistent with the pressure distributions computed using the Baldwin–Lomax[14] turbulence model (see Figs. 6 and 9).

The oil-flow patterns presented in Figs. 7 and 12, the pressure measurements presented in Fig. 11, and the computations presented in Fig. 8 can be used to develop a conceptual model of the flowfield in the viscous/inviscid interaction region just upstream of the compression ramp. The compression ramp that represents the closed inlet is at 37.7 deg relative to the approach supersonic flow. The shock-wave system required to turn the flow interacts with the approach boundary layer, creating a λ-shock-wave system, which turns the flows in increments and which causes a large adverse pressure gradient, leading to boundary-layer separation. The airflow in the shear layer at the outer edge of the separation region reattaches approximately midway up on the compression ramp (see the lines labeled air shear in Fig. 12c). However, because the compression ramp has a height h to width $2y_f$ ratio of 0.1667, three-dimensional effects are significant. The relief provided by the close proximity of the edges of the compression ramp causes the streamlines at the outer edge of the separation region to diverge slightly away from the plane of symmetry. As a result, there are two reattachment lines (one on either side of the plane of symmetry). The oil-flow patterns indicate

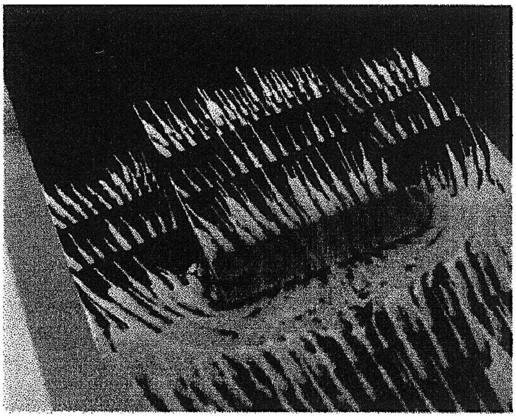

a) Photograph of SHMAC-I oil flow

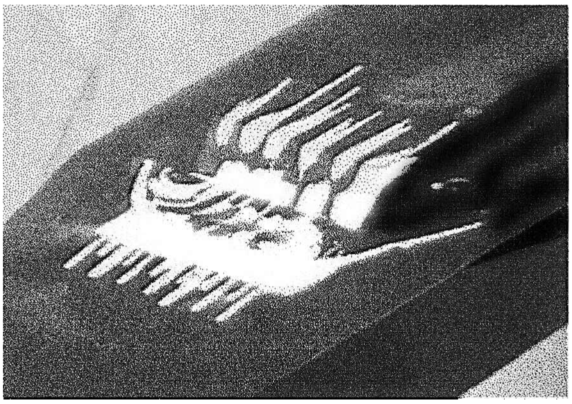

b) Photograph of SHMAC-II oil flow

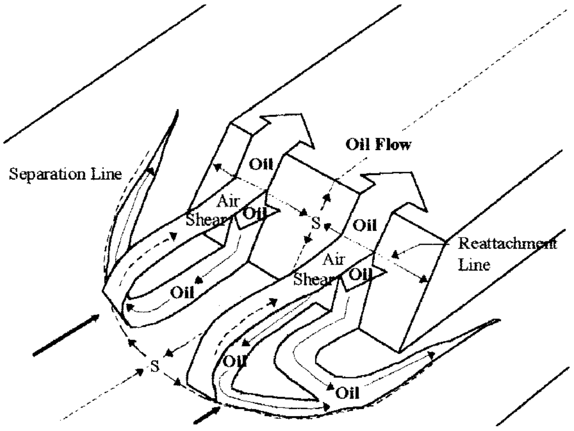

c) Conceptual model of the flowfield

Fig. 12 Flow in the interaction region.

that air flows toward the plane of symmetry from each of these interaction lines. This produces a saddle point, the point labeled "S" on the compression ramp in Fig. 12c. Another saddle point occurs at the separation point in the plane of symmetry, as indicated by an "S" on the forebody surface in Fig. 12c.

Consider a hypothetical air particle near the surface of the compression ramp starting from a point near (but not in) the plane of symmetry and below the reattachment line. Moving roughly parallel to the plane of symmetry, the air particle moves down the face of the compression ramp onto the forebody surface. As it nears the separation line, a strong pressure gradient in the y direction causes it to move away from the plane of symmetry. Nearing the separation line, it is entrained by the shear layer at the outer edge of the separated region. Because the air particle has entered the shear layer away from the plane of symmetry, it moves downstream toward the reattachment line with a significant y component of velocity. Because the original location of the air particle was inside the separated region, it remains in the separated region. Each time it repeats the recirculation path, it moves closer to the corner and is subjected to stronger pressure gradients. Thus, the air particle moves in a corkscrew pattern.

Concluding Remarks

Surface-pressure measurements and flow-visualization photographs have been obtained on a 0.079-scale model of a hypersonic cruise missile during an experimental program conducted in the TWT at USAFA. Data were obtained at a freestream Mach number of 4.28 and at a freestream Reynolds number (based on the model length) of 12.79×10^6 over an angle-of-attack range from -7.3 to $+7.3$ deg. The data are compared with computations made with GASPv3. The following conclusions are made based on the measurements and the computations for the range of conditions considered.

1) The flow in the viscous/inviscid interaction region caused by the shock-wave/boundary-layer interaction at the closed inlet was a complex, three-dimensional flow structure containing vortices with air particles following a corkscrew pattern.

2) The extent of the separated region in the plane of symmetry was greatest at an angle of attack of -7.3 deg and decreased continuously until the angle of attack was $+7.3$ deg.

3) Upstream of the interaction region, the experimentally determined streamwise pressure distribution in the plane of symmetry for an α of -7.3 deg was in excellent agreement with the computations made assuming that the flow was two dimensional.

4) Upstream of the interaction region, the pressures measured at an α of $+7.3$ deg decreased with distance from the nose of the model as compared with the two-dimensional computed pressures, which were independent of position. Thus, it appears that there were significant three-dimensional effects in the actual flowfield at this angle of attack.

Acknowledgments

The authors would like to thank the following organizations and people for their contributions to this effort. The U.S. Air Force Wright Laboratory is acknowledged both for the financial support of the experimental program through the HyTech Program Office and for the technical guidance and editorial input of Donald J. Stava. The Deutschen Forschungsgemeinschaft provided financial support. The Department of Defense High Performance Computing Center, the Naval Oceanographic Office, and the NASA Stennis Space Center provided partial support with Cray C-90 time. James E. Mayhew computed thermodynamic properties associated with the tunnel flow. Both Larry Lamblin, the tunnel technician, and Bobby Hatfield, the model builder, displayed dedication and competence critical to the successful execution of the test program. Viresh K. Wickramasinghe and Timothy Hayden are acknowledged for working with the spreadsheets used in the analysis of the data.

References

[1] Matthews, S., McIntyre, T., Taylor, J., Williamson, R., Boehm, J., Rasmussen, B., Sitler, A., Patrick, K., and Weiss, G., "A Hypersonic Attack Platform: The S^3 Concept," AIAA Paper 96-4580, Nov. 1996.

[2] Gregoire, J. E., and Krieger, R. J., "Aerodynamic Prediction Rationale for Advanced Arbitrary Shaped Missile Concepts," AIAA Paper 80-0256, Jan. 1980.

[3] Horstman, C. C., "Prediction of Hypersonic Shock-Wave/Turbulent-Boundary-Layer Interaction Flows," AIAA Paper 87-1367, June 1987.

[4] Dolling, D. S., "Problems in the Validation of CFD Codes Through Comparison with Experiment," *Theoretical and Experimental Methods in Hypersonic Flows*, CP-514, AGARD, 1993 (Paper 19).

[5] Simeonides, G., Haase, W., and Manna, M., "Experimental, Analytical, and Computational Methods Applied to Hypersonic Compression Ramp Flows," *Theoretical and Experimental Methods in Hypersonic Flows*, CP-514, AGARD, 1993 (Paper 22).

[6] Thomas, J. L., Dwoyer, D. L., and Kumar, A. J., "Computational Fluid Dynamics for Hypersonic Airbreathing Aircraft," *Hypersonic Flows for Reentry Problems*, edited by J. A. Desideri, R. Glowinski, and J. Periaux, Vol. 1, Springer–Verlag, Berlin, 1991, pp. 55–71.

[7] Delery, J., and Coet, M. C., "Experiments on Shock-Wave Boundary Layer Interactions Produced by Two-Dimensional Ramps and Three-Dimensional Obstacles," *Hypersonic Flows for Reentry Problems*, edited by J. A. Desideri, R. Glowinski, and J. Periaux, Vol. 2, Springer–Verlag, Berlin, 1991, pp. 97–111.

[8] AeroSoft, Inc., "General Aerodynamic Simulation Program," *Version 3 User's Manual*, Blacksburg, VA, May 1996.

[9] Bertin, J. J., Towne, M. C., Malan, M. A., Kreins, A. F., Zuber, M. E., and Parks, M. B., "Viscous/Inviscid Interactions of the Forebody Flowfield of an Airbreathing Hypersonic Vehicle," AIAA Paper 97-0766, Jan. 1997.

[10] Bertin, J. J., *Hypersonic Aerothermodynamics*, AIAA Education Series, AIAA, Washington, DC, 1994, pp. 58, 59.

[11] Dolling, D. S., "Considerations in the Comparison of Experimental Data with Simulations—Consistency of Math Models and Flow Physics," AIAA Paper 96-2030, June 1996.

[12] Kline, S. J., and McClintock, F. A., "Describing Uncertainties in Single-Sample Experiments," *Mechanical Engineering*, Vol. 75, Jan. 1953, pp. 3–8.

[13] Steinbrenner, J. P., and Chawner, J. R., "The GRIDGEN Version 9 Multiple Block Grid Generation Software," MDA Engineering, Inc., MDA Engineering Rept. 94-01, Arlington, TX, Aug. 1994.

[14] Baldwin, B. S., and Lomax, H., "Thin Layer Approximation and Algebraic Model for Separated Turbulent Flows," AIAA Paper 78-257, Jan. 1978.

[15] Jones, W. P., and Launder, B. E., "The Prediction of Laminarization with a Two-Equation Model of Turbulence," *International Journal of Heat and Mass Transfer*, Vol. 15, No. 2, 1972, pp. 301–314.

[16] Wilcox, D. C., *Turbulence Modeling for CFD*, 2nd ed., DCW Industries, La Cañada, CA, 1994, pp. 15–34.

[17] Ames Research Staff, "Equations, Tables, and Charts for Compressible Flow," NACA Rept. 1135, 1953.

B. A. Bhutta
Associate Editor